buildings

Article

Machine Learning-Based Strength Prediction of Round-Ended Concrete-Filled Steel Tube

Dejing Chen [1,2,3], Youhua Fan [2] and Xiaoxiong Zha [1,2,3,*]

1. School of Civil and Environmental Engineering, Harbin Institute of Technology, Shenzhen 518055, China; chendejin0302@163.com
2. School of Science, Harbin Institute of Technology, Shenzhen 518055, China; yhfan@hit.edu.cn
3. Guangdong Provincial Key Laboratory of Intelligent and Resilient Structures for Civil Engineering, Shenzhen 518055, China

* Correspondence: zhaxx@hit.edu.cn

Abstract: Round-ended concrete-filled steel tubes (RECFSTs) present very different performances between the primary and secondary axes, which renders them particularly suitable for use as bridge piers and arches. In recent years, research into RECFST heavily relies on experimental procedures restricting the parameter range under consideration, which narrows the far-reaching applicability of RECFST. This study employs advanced machine learning methods to predict the axial load-bearing capacity of RECFST with a wide parameter range. Firstly, a machine learning database comprising 2400 RECFSTs is established, which covers a wider range of commonly used material strengths and cross-sectional dimensions. Three machine learning prediction models of this database are then developed, respectively, using different algorithms. The robustness of the machine learning models is evaluated by predicting the axial load-bearing capacity of 60 RECFST specimens from existing references. The results demonstrated that the machine learning models provided superior predictive accuracy compared to theoretical or code-based formulas. A graphical user interface (GUI) is ultimately developed based on the machine learning prediction models to predict the axial load-bearing capacity of RECFST. This tool facilitates rapid and accurate RECFST design.

Keywords: round-ended concrete-filled steel tube; machine learning method; strength prediction; graphical user interface

check for updates

Citation: Chen, D.; Fan, Y.; Zha, X. Machine Learning-Based Strength Prediction of Round-Ended Concrete-Filled Steel Tube. *Buildings* **2024**, *14*, 3244. https://doi.org/10.3390/buildings14103244

Received: 7 September 2024
Revised: 6 October 2024
Accepted: 11 October 2024
Published: 13 October 2024

1. Introduction

A round-ended concrete-filled steel tube (RECFST) not only retains the excellent load-bearing capacity, ductility, and ease of construction associated with traditional circular concrete-filled steel tubes, but it is also suitable for applications requiring enhanced resistance along a single axis of the section. Compared to rectangular concrete-filled steel tubes [1,2], RECFSTs offer lower fluid resistance, making them advantageous in structures such as bridges exposed to fluid loads. Additionally, the combination of "arc" and "straight" edges enhances both versatility and esthetics in structural design, which has led to its increasing use in practical engineering. Notable examples in China include the Houhu Bridge in Wuhan, the Shennong Bridge (formerly Weihe Bridge) in Baoji, and the Qixia Bridge in Nanjing, as illustrated in Figure 1.

Lu et al. [3–6] were among the pioneers in studying the performance of RECFST. Their research primarily focused on the axial performance, eccentricity performance, design methodology, and construction techniques of RECFST columns, which were implemented in the Houhu Bridge.

Subsequently, numerous studies have been conducted on this topic. Wang et al. [7,8] investigated the axial and bending performance of RECFST. Ding et al. [9–11] extended this work by performing a reliability analysis of the bearing capacity in addition to their research on axial and bending performance. Wang et al. [12–16] conducted a comprehensive series of studies on the axial, eccentric, hysteretic, and node connection performance. Zhao et al. [17–20] contributed with studies on axial and bending performance under impact, slender columns under compression, and ongoing research on the axial performance of RECFST components utilizing recycled aggregate concrete. Ren et al. [21] focused on the axial and eccentric performance of short- and medium-length columns, examining the influence of cross-sectional parameters on component performance. Hassanein and Patel [22] conducted a finite element study on axial performance, while Piquer et al. [23] performed experimental research on eccentric performance, incorporating an analysis of high-strength concrete. To improve the efficiency of finite element calculations, researchers such as Patel [24], Zhang [25], and Ahmed [26,27] developed a finite element model for RECFST based on the fiber beam element.

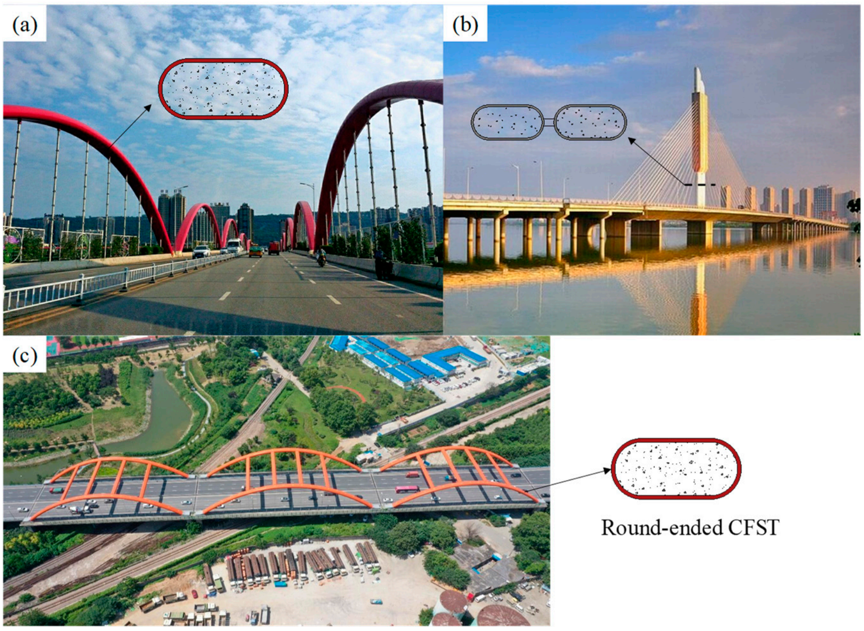

Figure 1. Application of RECFST: (**a**) Houhu Bridge; (**b**) Weihe Bridge; (**c**) Qixia Bridge.

Axial performance, as a fundamental aspect of RECFST, has received significant attention in the aforementioned research. Wang et al. [7], Ding et al. [10], Ren et al. [21], and Hassanein et al. [22] proposed calculation formulas for the axial compression-bearing capacity of RECFST. However, these formulas are limited by specific parameter ranges, and their prediction accuracy outside these ranges requires further investigation. Consequently, there is a need for a new calculation method for RECFST bearing capacity that can accommodate a wider range of parameters.

With the advent of the big data era, machine learning, a key branch of artificial intelligence, is widely used to solve various prediction, classification, and clustering problems [28]. In recent years, machine learning has increasingly been applied in structural engineering [29,30], with numerous researchers utilizing these techniques to predict the bearing capacity of concrete-filled steel tubes (CFSTs). While most machine learning studies focus on circular CFST [31–36], other cross-sectional shapes, such as square, rectangular, and elliptical, have also been investigated [37–44]. These studies primarily address axial performance, though some also explore other loading conditions [45–50], including eccentric compression, bending, and torsion. The research encompasses various CFST types, such as concrete-filled double-skin tubes [51,52], FRP-CFST [53,54], CFST with recycled aggregate concrete [55], and concrete-encased CFST [56]. Most machine learning studies [31–42,44,46,47,49,53,55] use experimental data for training, while some incorporate both experimental data and finite element models [43,48,50–52,54], or rely solely on finite element models [45]. The integration of machine learning with the mechanical performance of CFST has opened new avenues for the field, offering fresh insights into the study of RECFST performance.

This study employs three advanced machine learning techniques to predict the axial load-bearing capacity of RECFST. Using a validated finite element modeling (FEM) method and within the commonly used parameter range for RECFST structures, 2400 FEM models were developed to determine their axial load-bearing capacities. These models formed the basis of a machine learning database, with 80% of the data allocated for training and 20% for testing. Hyperparameter optimization for the three machine learning techniques was performed using grid search methods combined with fivefold cross-validation. The optimized prediction models were subsequently applied to predict the axial load-bearing capacity of 60 collected RECFST specimens. The results were compared with those derived from the existing standards and theoretical formulas, demonstrating superior accuracy. Finally, a graphical user interface (GUI) was created, incorporating the optimal prediction models to facilitate the rapid and accurate calculations of the axial load-bearing capacity of RECFST structures. The research flow of this study is illustrated in Figure 2.

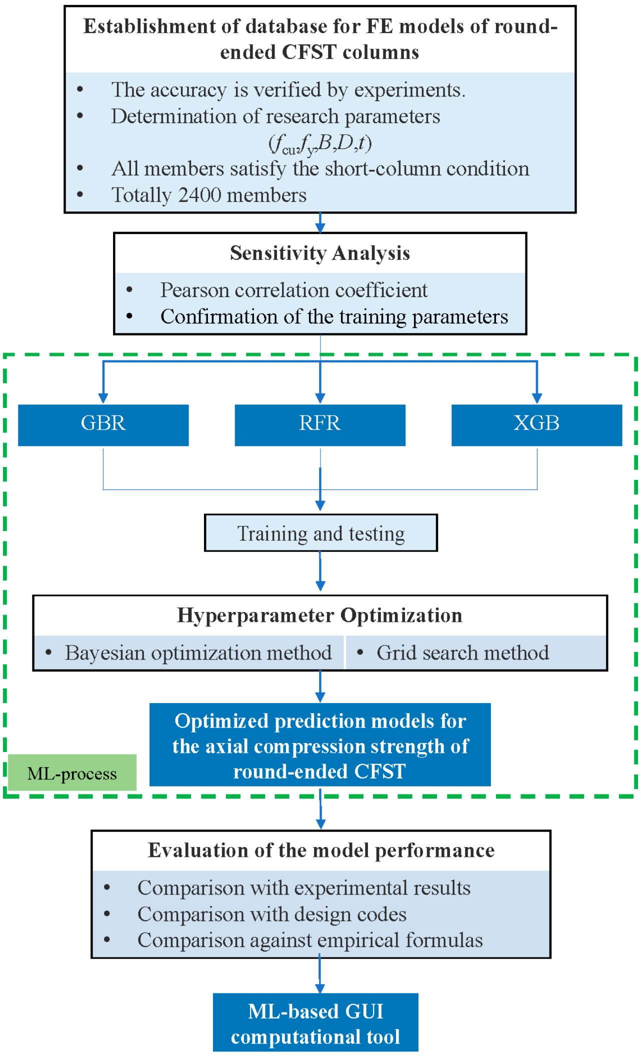

Figure 2. Research flow.

2. Database Establishment

As is known, the performance of the predictive model in machine learning is better with a larger sample size. The number of experimental samples of RECFSTs currently available for retrieval is relatively limited because research on RECFSTs has only begun to gain traction in recent years. By selecting an appropriate parameter range, a database of 2400 RECFST finite element (FE) models was established, and the axial compression-bearing capacity data were obtained to facilitate machine learning for predicting the load-bearing capacity.

2.1. Finite Element Model

This study selects specimens from different references as reference samples, namely WST1-A from Ref. [10], RR-1-180-6 from Ref. [21], and RCFST-1 from Ref. [7]. The cross-sectional dimensions and material strength information of the above three specimens are shown in Figure 3 and Table 1. The finite element models of these three specimens were established, and the validity of the finite element modeling method was verified by comparing them to the experimental results.

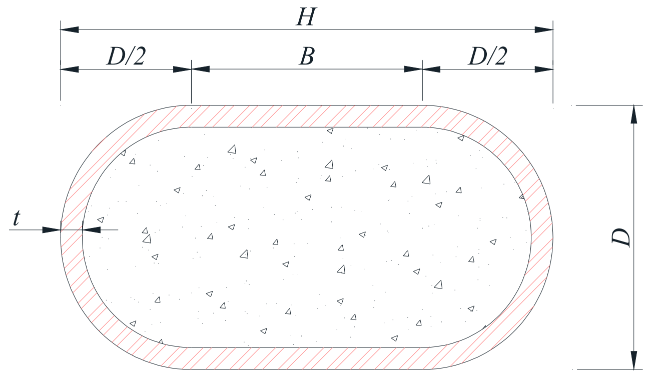

Figure 3. Cross-section of RECFST.

Table 1. Cross-sectional information of selected specimens.

Specimens	f_{cu}	f_y	B	D	t	N_{u_test}	N_{u_FE}	N_{u_FE}/N_{u_test}
WST1-A	40.4	327.7	47	252	3.75	3429	3395.56	0.990
RR-1-180-6	31	290	150	160	6	2319	2388.66	1.030
RCFST-1	38.06	324.6	51.5	117	2.86	925	988.265	1.068

2.1.1. Selection of Elements and Mesh Division

RECFST can be divided into exterior steel tubes and core concrete. In this paper, the shell element S4R is used to simulate the exterior steel tubes, and the solid element C3D8R is used to simulate the core concrete. Both the concrete and the steel tube have the same mesh size settings. To quickly establish a parametric finite element database, the mesh size (l_{mesh}) is set to 1/10 of the short side of the section, i.e., l_{mesh} = 0.1 × min (H, D), indicating that at least 10 grids have been divided in one direction of the specimen section. The mesh division of the specimen is shown in Figure 4. To ensure mesh size convergence, the mesh number was doubled, and the results were compared. The small difference between the results (within 1%) suggests that the mesh size (l_{mesh}) satisfies the accuracy requirements.

2.1.2. Material and Constitutive Properties

(1) Concrete

In this study, the Concrete Damaged Plasticity (CDP) model in the ABAQUS software (Version 6.14) is used for simulating the concrete. The specific parameters in the CDP model include dilation angle, eccentricity, f_{b0}/f_{c0}, K, and viscosity parameter, which are calibrated and set as 23, 0.1, 1.16, 0.667, and 0.0001, respectively.

The confinement of the enclosing steel tube greatly enhances the compression behavior and strength of the core concrete in CFST. This enhancement necessitates a reliance on confined concrete constitutive models for accurate representation. The strength of confined concrete depends on the level of confinement, which in CFST primarily comes from the shape of the outer steel tube. Circular CFSTs provide substantial confinement through the interaction between the steel tube and concrete, significantly enhancing the strength of the core concrete. In contrast, square or rectangular CFSTs offer less confinement, resulting in a more modest increase in core concrete strength. The cross-sectional shape of RECFST is intermediate between circular and rectangular configurations. According to Wang's study [14], when the aspect ratio (H/D) exceeds 1.44, the strength evolution of the core concrete in RECFST resembles that of rectangular CFST. In contrast, when the aspect ratio is 1.44 or lower, the strength progression of the core concrete is similar to that of circular CFST.

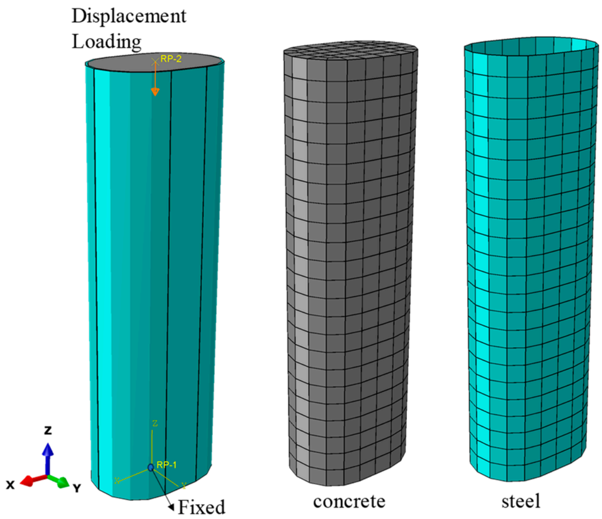

Figure 4. Mesh division of the specimen.

The concrete constitutive model in this study is classified into two scenarios: when $H/D > 1.44$, the confined concrete constitutive for rectangular CFST is adopted; when $H/D \leq 1.44$, the circular CFST model is applied. The constitutive relationships for confined concrete, referenced as [57], are presented in Equations (1)–(7).

$$y = \begin{cases} 2x - x^2 & (x \leq 1) \\ \frac{x}{\beta_0 (x-1)^{\eta} + x} & (x > 1) \end{cases} \tag{1}$$

$$x = \frac{\varepsilon}{\varepsilon_0}\ y = \frac{\sigma}{\sigma_0} \tag{2}$$

$$\sigma_0 = f_{\mathrm{c}}' \tag{3}$$

$$\varepsilon_0 = \varepsilon_{\mathrm{c}} + 800\xi^{0.2} \times 10^{-6} \tag{4}$$

$$\varepsilon_{\mathrm{c}} = (1300 + 12.5 f_{\mathrm{c}}) \times 10^{-6} \tag{5}$$

$$\eta = \begin{cases} 2 & (H/D < 1.44) \\ 1.6 + 1.5/x & (H/D \geq 1.44) \end{cases} \tag{6}$$

$$\beta_0 = \begin{cases} \left(2.36 \times 10^{-5}\right)^{\left[0.25 + (\xi - 0.5)^7\right]} \times (f_c')^{0.5} \times 0.5 \geq 0.12 & (H/D < 1.44) \\ \frac{(f_c')^{0.1}}{1.2\sqrt{1+\xi}} & (H/D \geq 1.44) \end{cases} \tag{7}$$

For the tensile constitutive model of concrete, the concrete fracture energy (G_{f})–cracking displacement (u_{t}) relationship model provided in the CDP model has better computational convergence [58]. Therefore, the fracture energy cracking criterion (GFI) is used in this paper to describe the tensile constitutive relationship of concrete.

The fracture energy of concrete refers to the energy required to extend the crack per unit area. The concrete fracture energy G_f is calculated according to the following equation [59]:

$$G_f = a \cdot (\frac{f_c'}{10})^{0.7} \times 10^{-3} \tag{8}$$

$$a = 1.25d_{max} + 10 \tag{9}$$

where d_{max} is the particle size of the coarse aggregate in the concrete; $f_c{}'$ is the compressive strength of the concrete cylinder.

The peak tensile stress σ_p of the concrete is calculated according to the following formula [60]:

$$\sigma_p = 0.26(1.5f_{ck})^{2/3} \tag{10}$$

In which, f_{ck} is the standard value of the axial compressive strength of concrete (MPa); the relationship between stress and displacement after the concrete cracks is shown in Figure 5.

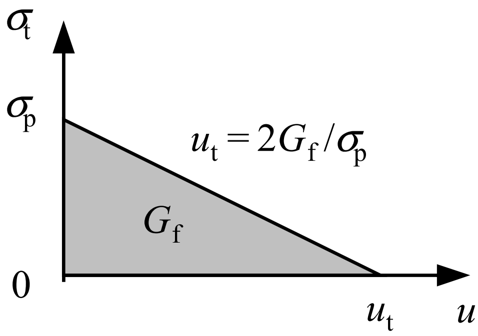

Figure 5. Relationship between G_f and u_t.

(2) Steel

Assuming that steel is an isotropic material, for its elastic stage performance, it is necessary to define Young's model and Poisson's ratio. In this paper, Young's modulus E_s and Poisson's ratio v are taken to be 206 GPa and 0.3, respectively.

In the event of steel transitioning into the plastic working state, researchers currently adopt various stress–strain models, encompassing the ideal elastic–plastic model [61] and the elastic–plastic model featuring a strain hardening section [62,63]. For this study, Han's five-stage stress–strain relationship [57] was implemented as the constitutive model for steel, as shown in Equations (11)–(13). This model encompasses elasticity, elasto-plasticity, plasticity, hardening, and fracture stages, as graphically represented in Figure 6.

$$\sigma_s = \begin{cases} E_s\varepsilon_s & \varepsilon_s \le \varepsilon_e \\ -A\varepsilon_s{}^2 + B\varepsilon_s + C & \varepsilon_e < \varepsilon_s \le \varepsilon_{e1} \\ f_y & \varepsilon_{e1} < \varepsilon_s \le \varepsilon_{e2} \\ f_y[1 + 0.6\frac{\varepsilon_s - \varepsilon_{e2}}{\varepsilon_{e3} - \varepsilon_{e2}}] & \varepsilon_{e1} < \varepsilon_s \le \varepsilon_{e2} \\ 1.6f_y & \varepsilon_s > \varepsilon_{e3} \end{cases} \tag{11}$$

$$\varepsilon_e = 0.8f_y/E_s,\ \varepsilon_{e1} = 1.5\varepsilon_e,\ \varepsilon_{e2} = 10\varepsilon_{e1},\ \varepsilon_{e3} = 100\varepsilon_{e1} \tag{12}$$

$$A = 0.2f_y/(\varepsilon_{e1} - \varepsilon_e)^2,\ B = 2A\varepsilon_{e1}\ ,\ C = 0.8f_y + A\varepsilon_e^2 - B\varepsilon_e \tag{13}$$

2.1.3. Contact and Boundary Conditions

In the finite element simulations of steel structures or concrete-filled steel tube structures, it is sometimes necessary to simulate welds [64] in order to accurately represent the structural form. However, when the focus of the study is not on the welds, for the sake of convenience, it is often assumed that no failure occurs at the welds. As a result, welds are not considered in the model, simplifying the finite element model. This paper follows the latter approach. For the contact between the steel tube and the concrete, normal "hard" contact and tangential penalty functions can usually be set for modeling. Additionally, there is also a method to directly "tie" the inside surface of the steel tube to the outside surface of the concrete. In the axial compression of CFST stub columns, the interaction between the steel tube and concrete primarily involves mutual squeezing, with tangential relative slippage occurring rarely. According to Yu's research [65], little difference exists in the axial load-bearing capacity of CFST using the above two methods for simulating contact between steel and concrete. Consequently, in this paper, the "tie" contact is used.

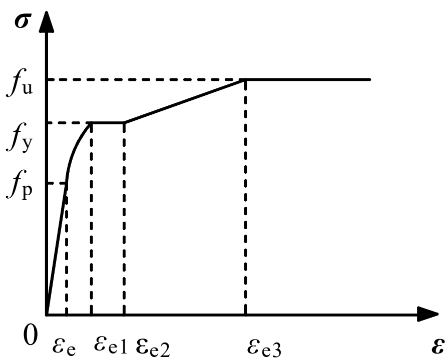

Figure 6. Constitutive relation model of steel.

Reference points, termed as RP-Top and RP-Bottom, are established at the top and bottom of the component, respectively. The RP-Top is rigidly attached to the top steel tube and concrete node, and similarly, the RP-Bottom is rigidly fastened to the bottom steel tube and concrete node. This configuration establishes a relationship between the degrees of freedom at the component's top and bottom and their respective reference points, RP-Top and RP-Bottom. Through the allocation of the degrees of freedom for RP-Top and RP-Bottom, the boundary conditions for the component are effectively established. The finite element models of the three specimens are shown in Figure 7. In experiments, the base of the specimen is typically fixed, while the top is either hinged or free. According to Refs. [66,67], these boundary conditions have minimal impact on the axial bearing capacity of the stub column. Therefore, in this study, the finite element model is uniformly defined with a fixed bottom and a free top. In this paper, a general static analysis type is used, applying axial displacement loads to the reference point at the top of the column (RP-Top) to simulate the axial compression process of the RECFST.

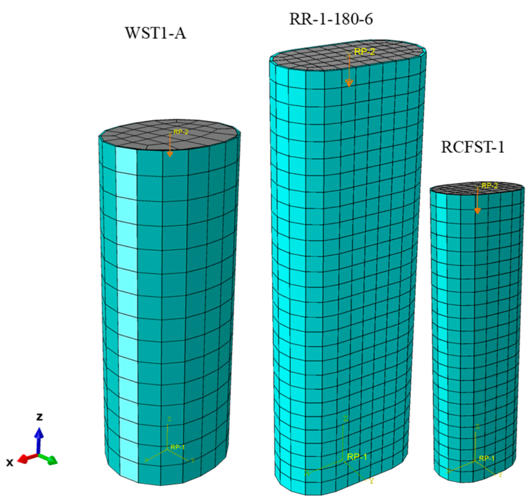

Figure 7. Finite element models of the three selected specimens.

2.2. Verification of FE Model

The load–deformation curves of the three specimens obtained from the finite element model are compared with the measured curves in the Refs. [7,10,21], as shown in Figure 8. As can be seen from the figure, apart from some differences in the descending segment, the finite element curve fits well with the measured curve, including its initial stiffness and peak load, which are quite close.

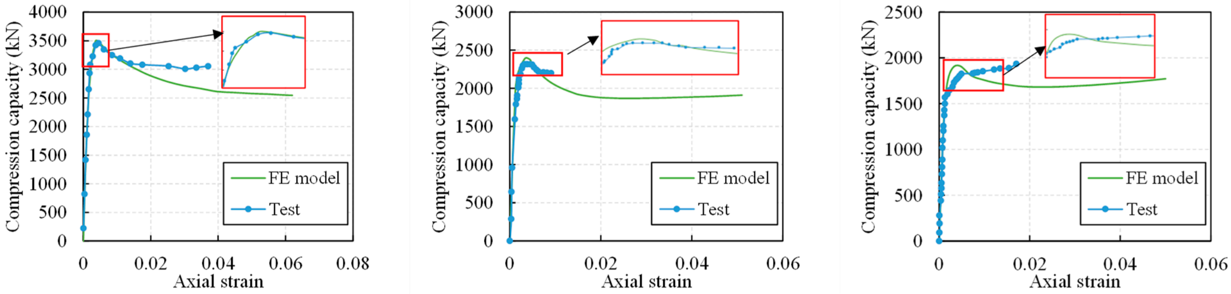

(**a**) WST1-A (**b**) RR-1-180-6 (**c**) RCFST-1

Figure 8. Comparison between FE model and tests.

Table 1 shows a comparison of the measured peak loads of the three specimens and the results calculated from the finite element model. The measured peak loads of the specimens WST1-A, RR-1-180-6, and RCFST-1 are, respectively, 3429 kN, 2319 kN, and 925 kN, while the finite element calculation results are 3395.56 kN, 2388.66 kN, and 988.27 kN, with errors of −0.96%, 3.00%, and 6.84%, respectively. Judging from the load–deformation curves and the comparison results of the peak load, the established finite element model can well simulate the axial compression process of RECFST, especially in calculating its axial bearing capacity with better accuracy.

2.3. Establishment of Machine Learning Database

This paper employs a validated finite element modeling method to create numerous finite element models of RECFST under axial compression for machine learning purposes. According to Chinese code GB50017-2017 [68], commonly used steel grades in mainland China include Q235, Q355, Q390, Q420, and Q460, corresponding to the yield strengths of f_y = 235, 355, 390, 420, and 460 MPa, respectively. Likewise, commonly used concrete strengths [69] are f_{cu} = 30, 40, 50, 60, 70, and 80 MPa. Thus, the established finite element database in this study should include the aforementioned material strengths.

The selected cross-sectional dimensions for RECFST columns are D = 100, 300, 500, and 700 mm; B = 100, 300, 500, and 700 mm; and t = 2, 4, 6, 8, and 10 mm. These dimensions are widely used in engineering applications and encompass most current engineering data. Ref. [70] notes that as the slenderness ratio of a component increases, its failure mode shifts from sectional strength failure to overall instability under axial load, significantly reducing its axial bearing capacity. This scenario differs from the strength concerns primarily addressed in this paper. Thus, to avoid overall instability when establishing the finite element database, the component length is uniformly set to $L = 3 \times \min(D, H)$.

In summary, the parameters changing in the finite element model database established in this paper for the RECFST stub column are f_{cu} = 30, 40, 50, 60, 70, 80 MPa; f_y = 235, 355, 390, 420, 460 MPa; D = 100, 300, 500, 700 mm; B = 100, 300, 500, 700 mm; t = 2, 4, 6, 8, 10 mm. A grid combination, demonstrated in Figure 9, is utilized, and all the parameters have been extensively examined. This has resulted in the establishment of $6 \times 5 \times 4 \times 4 \times 5 = 2400$ finite element models, thereby forming the database for machine learning around the axial compression-bearing capacity of RECFST. By using the core language Python 2.7 in ABAQUS 6.14, parameterized modeling code was developed to automate the modeling of the 2400 finite element models, significantly reducing the time required for manual operations.

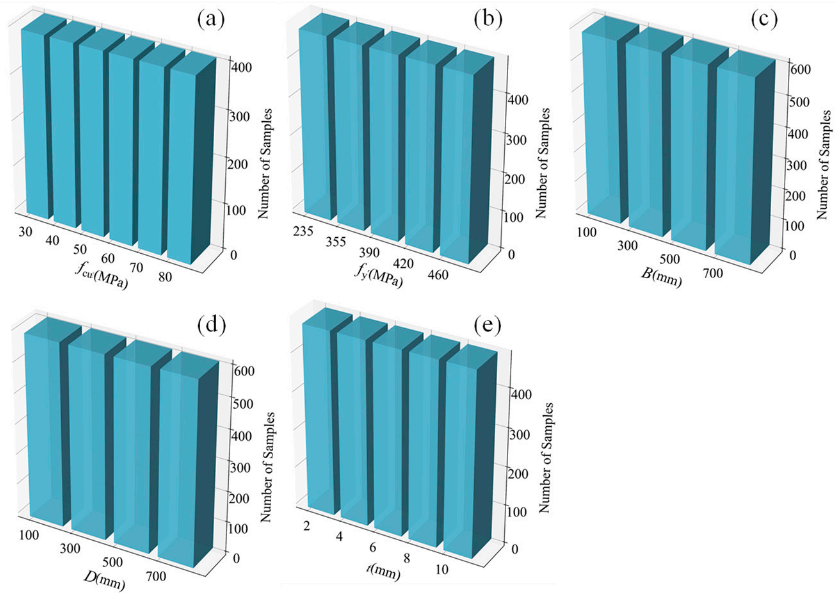

Figure 9. Statistical distributions of the parameters for the RECFSTs: (**a**) f_{cu}; (**b**) f_y; (**c**) B; (**d**) D; (**e**) t.

3. Machine Learning

3.1. Sensitivity Analysis

The key parameters of the RECFST stub columns are f_{cu}, f_y, D, B, and t. These parameters collectively define all the properties of a RECFST, encompassing the cross-sectional shape and material strength, thereby determining the axial compression-bearing capacity of the RECFST. Hence, these variables are known as the primary parameters. In addition, there are some parameters that also have a significant impact on the axial compression bearing capacity of RECFST. These parameters are formed by the combination of the primary parameters and are referred to as the secondary parameters, such as A_s, A_c, A_sf_y, A_cf_{cu}, $A_sf_y/(A_cf_{cu})$, and D/B. A sensitivity analysis of both the primary and secondary variables regarding the axial compression-bearing load is conducted to improve the prediction accuracy of the machine learning model, aiding in the selection of parameters for the final training model.

Correlation analysis is a statistical method that can quantify the correlation between two variables. The Pearson correlation coefficient [71] is defined as follows:

$$r = \frac{n\sum_{i=1}^{n} x_i y_i - \sum_{i=1}^{n} x_i \sum_{i=1}^{n} y_i}{\sqrt{n\sum_{i=1}^{n} x_i^2 - \left(\sum_{i=1}^{n} x_i\right)^2}\sqrt{n\sum_{i=1}^{n} y_i^2 - \left(\sum_{i=1}^{n} y_i\right)^2}} \tag{14}$$

where x_i and y_i represent the two calculation parameters, and n is the total number of samples. The closer r is to 1, the stronger the positive correlation; the closer r is to 0, the weaker the correlation; and the closer r is to -1, the stronger the negative correlation.

Figure 10 shows the Pearson correlation coefficient between each parameter, in the figure, a deeper shade of green indicates a stronger correlation. In addition to the primary parameter that determines the properties of RECFST, the second parameters such as A_cf_{cu}, $A_c + A_s$, A_c, A_s, A_sf_y, etc., all show a large correlation with the axial compressive capacity N_u, with their Pearson coefficients being 0.968, 0.909, 0.904, 0.694, and 0.684, respectively, as shown in Figure 11. This is relatively in line with the calculation formulas of the standards of various countries [72–74] and the empirical formulas [10,21,22]. Most of these calculation formulas contain the abovementioned secondary parameters, as listed in Table 2.

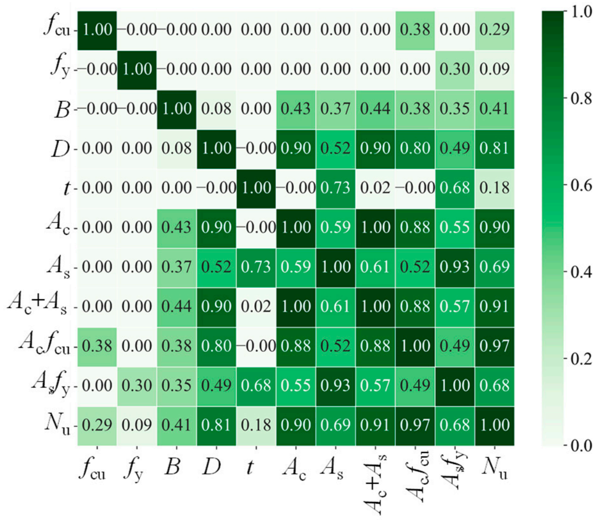

Figure 10. Correlation analysis between different parameters.

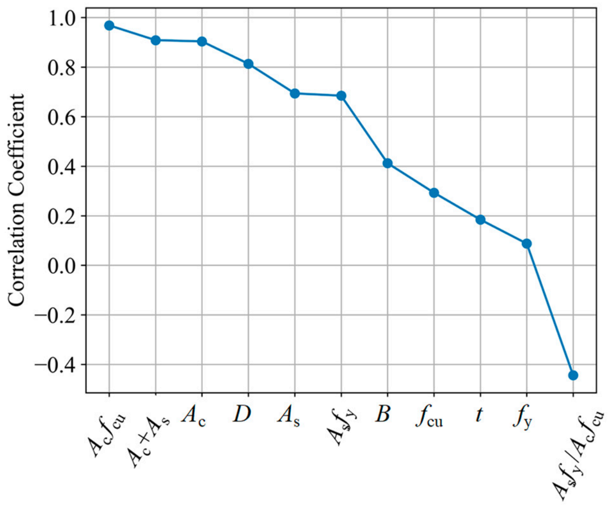

Figure 11. Correlation coefficient between ultimate capacity and different parameters.

Table 2. Comparison of input parameters between the empirical formulas and existing standards.

Calculation Model	A_s	A_c	$A_c f_{cu}$ or $A_c f_c$ or $A_c f_{c'}$	$A_s f_y$	$A = A_s + A_c$	$A_s f_y / A_c f_{cu}$
Ding [10]	×	√	√	×	×	√
Ren [21]	×	√	√	×	×	√
M.F. Hassanein [22]	×	×	×	×	×	×
ACI318-11 [72]	×	×	√	√	×	×
GB 50936-2014 [73]	×	×	×	×	√	√
AISC 360-16 [74]	×	×	√	√	×	×

Based on the outcomes of the sensitivity analysis and insights from the existing calculation methods, this study employs the following parameters as input for machine learning training: f_{cu}, f_y, D, B, t, $A_c f_{cu}$, and $A_s f_y$. The primary parameters, which define the cross-sectional geometry and material strength of RECFST, are f_{cu}, f_y, D, B, and t. $A_c f_{cu}$ and $A_s f_y$ serve as the secondary parameters, representing the independent compression capacity of concrete and steel tube, respectively.

3.2. Selected Algorithm

3.2.1. Gradient Boosting Regression (GBR)

Gradient Boosting Regression (GBR) is an ensemble learning method which builds a powerful predictive model by combining multiple weak learners. In its simplest form, these weak learners can be decision trees, but other learning algorithms can also be used. The core idea of this method is that each new model strives to correct the prediction errors of all the previous models. The main advantage of GBR is that it can handle various types of prediction problems (including classification, regression, etc.), and can naturally handle mixed types of features (i.e., different types of features such as categories and numbers in the same data set). In addition, GBR has strong robustness to missing values and outliers.

3.2.2. Random Forest Regression (RFR)

The random forest regression (RFR) algorithm is an important application branch of random forest. The random forest regression model obtains prediction results in parallel by randomly sampling and extracting features to build many unrelated decision trees. Each decision tree can obtain a prediction result through the extracted samples and features, and the regression prediction result of the entire forest can be obtained by averaging the results of all the trees. The main advantage of RFR is that it hardly requires input preprocessing, can handle high-dimensional (i.e., a lot of features) data, and can handle missing values. Moreover, because of the use of ensemble learning, RFR is generally not prone to overfitting, and the model has strong robustness.

3.2.3. Extreme Gradient Boosting (XGB)

Extreme Gradient Boosting (XGB) is one of the most widely used machine learning algorithms. After Friedman [75] proposed this tree-based gradient boosting algorithm, it was improved and optimized by Chen and Guestrin [76], making XGB more efficient to operate and apply to a variety of problems.

The main architecture of XGB can be summarized into three parts: feature selection, tree building, and model optimization. The workflow of the entire architecture mainly consists of the following two stages: one is setting goals according to the loss function and making predictive output using tree-based models; the other is providing feedback based on the gap between the actual output and the expected output, and model optimization is carried out using gradient boosting algorithms.

One of the main features of XGB is its high degree of customizability and flexibility. In addition to the built-in objective functions, users can also set custom objective functions for optimization. At the same time, XGB incorporates regularization parameters to help prevent model overfitting and uses pruning technology. The impacts caused by model overfitting can be directly ignored, reducing the difficulty of model tuning.

3.3. Evaluation Metrics and Hyperparameter Optimization

3.3.1. Evaluation Metrics

The evaluation of the model's predictive performance generally involves the following parameters. In these equations [77], $N_{\mathrm{u}}^{\mathrm{FE}}$ and $N_{\mathrm{u}}^{\mathrm{ML}}$ are the axial compression bearing capacity RECFST obtained by the FE model and machine learning model, respectively.

(1) Coefficient of determination (R^2)

$$R^2 = \frac{\left[\sum_{i=1}^{n}\left(N_{\mathrm{ui}}^{\mathrm{FE}} - \overline{N_{\mathrm{u}}^{\mathrm{FE}}}\right)\left(N_{\mathrm{ui}}^{\mathrm{ML}} - \overline{N_{\mathrm{u}}^{\mathrm{ML}}}\right)\right]^2}{\left[\sum_{i=1}^{n}\left(N_{\mathrm{ui}}^{\mathrm{FE}} - \overline{N_{\mathrm{u}}^{\mathrm{FE}}}\right)^2\right]\left[\sum_{i=1}^{n}\left(N_{\mathrm{ui}}^{\mathrm{ML}} - \overline{N_{\mathrm{u}}^{\mathrm{ML}}}\right)^2\right]} \tag{15}$$

R^2 is between 0 and 1. The closer R^2 is to 1, the greater the correlation between the predicted value and the FE value, reflecting that the performance of the prediction model is better.

(2) Mean absolute error (*MAE*)

$$MAE = \frac{\sum_{i=1}^{n} \left| N_{\mathrm{ui}}^{\mathrm{ML}} - N_{\mathrm{ui}}^{\mathrm{FE}} \right|}{n} \tag{16}$$

MAE shows the error between the ML predicted value and the FE value and avoids the mutually offsetting problem between over-estimating errors and under-estimating ones. The smaller the *MAE*, the better the performance of the prediction model.

(3) Root mean square error (*RMSE*)

$$RMSE = \sqrt{\frac{\sum_{i=1}^{n} \left(N_{\mathrm{ui}}^{\mathrm{ML}} - N_{\mathrm{ui}}^{\mathrm{FE}} \right)^2}{n}} \tag{17}$$

RMSE is somewhat similar to *MAE*, both reflecting the error between the ML predicted value and the FE value. Because squaring amplifies the weights of larger errors, it is more sensitive to outliers. The smaller the *RMSE*, the better the predictive performance of the model.

(4) Mean (*MEAN*)

$$MEAN = \frac{\sum_{i=1}^{n} \left(N_{\mathrm{ui}}^{\mathrm{ML}} / N_{\mathrm{ui}}^{\mathrm{FE}} \right)}{n} \tag{18}$$

MEAN is the average of the ratio of the ML predicted value to the FE value. The closer it is to 1, the better the prediction performance of the model.

(5) Coefficient of variation (*COV*)

$$COV = \sqrt{\frac{\sum_{i=1}^{n} \left[N_{\mathrm{ui}}^{\mathrm{ML}} / N_{\mathrm{ui}}^{\mathrm{FE}} - MEAN \right]^2}{n}} / MEAN \tag{19}$$

COV reflects the degree of dispersion of the ratio of the predicted value to the FE value. The smaller the *COV*, the lower the degree of data dispersion. The closer the *MEAN* is to 1 and the smaller the *COV*, the better the predictive performance of the model.

3.3.2. Hyperparameter Optimization

To avoid overfitting, underfitting, or achieving local optimum problems for the above models, the grid search method combined with fivefold cross-validation is adopted to optimize the hyperparameters of the above models. The objective of optimization is with the smallest *MAE*. Taking the GBR model as an example, the key hyperparameter learning_rate is set as 0.01, 0.10, 0.5, and 1; n_estimators is set as 100, 200, 300, and 10,000; and max_depth is set as 2,3, 5, 10, and 20. The training set is randomly divided into 5 folds, of which 4 folds are used as the training set, and the remaining 1 fold is used as the validation set. All the combinations of the above key hyperparameters are traversed to obtain the best hyperparameters. The selection of key hyperparameter ranges and the optimal hyperparameter values for the three models are shown in Table 3.

3.4. Comparison of Results

The machine learning process implemented in this paper is all based on the Python platform, and all three models randomly select 80% of the sample size in the database as the training set, while the remaining 20% of the samples serve as the test set.

The calculated evaluation indexes of each model are shown in Table 4. The comparison of the coefficient of determination of each model is shown in Figure 12. For the training set, the R^2 of the three models all exceed 0.999. As for the test set, the XGB model achieves the best result, followed by GBR, and the R^2 of the RFR model is the smallest, at 0.9985.

Overall, whether it is the test set or the training set, the R^2 of the three models is quite close to one.

Table 3. Optimization of key hyperparameters.

ML Model	Key Hyperparameters Ranges	Best Key Hyperparameters
GBR	learning_rate: 0.01, 0.10, 0.5, 1 n_estimators: 100, 200, 300, 10,000 max_depth: 2,3, 5, 10, 20	learning_rate: 0.1 n_estimators: 300 max_depth: 5
RFR	n_estimators:10~1000 max_depth:1~20 min_samples_split: 2~11	n_estimators:43 max_depth: 20 min_samples_split: 2
XGB	learning_rate: 0.01, 0.10, 0.5, 1 n_estimators: 100, 200, 300, 10,000 max_depth: 2, 3, 5, 10, 20	learning_rate: 0.1 n_estimators: 10,000 max_depth: 5

Table 4. Evaluation index of the machine learning models.

ML Model	Evaluation Index				
	Coefficient of Determination (R^2) Training Set /Testing Set	Mean Absolute Error (MAE) Training Set /Testing Set	Root Mean Square Error (RMSE) Training Set /Testing Set	Mean (MEAN) Training Set /Testing Set	Coefficient of Variation (COV) Training Set /Testing Set
XGB	0.9998/0.9991	129/230	200/411	1.0011/1.0013	0.0091/0.0180
GBR	0.9995/0.9989	208/269	304/429	1.0005/1.0004	0.0188/0.0224
RFR	0.9997/0.9985	114/292	195/506	1.0002/0.9999	0.0091/0.0226

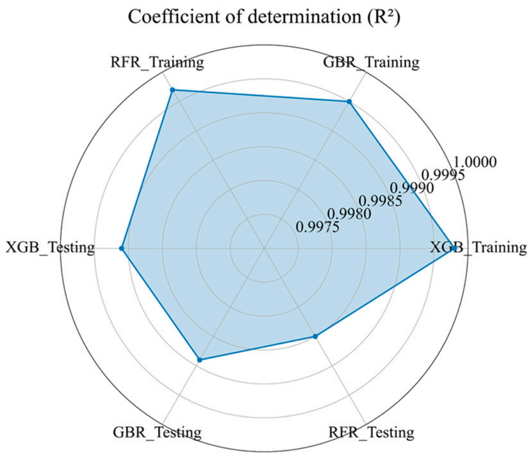

Figure 12. Coefficient of determination of different models.

Figure 13 shows the comparison of the *MAE* and *RMSE* of each model's training set and test set. It can be seen that the XGB model achieves better results in both the training set and test set, with the smallest *MAE* and *RMSE* in the test set among the three models. The RFR model performs best in the training set but performs worst in the test set (its *MAE* and *RMSE* in the training set are the smallest among the three models, but the largest in the test set). The GBR model performs worst in the training set but performs relatively well in the test set.

Figure 14 shows the comparison of the *MEAN* and *COV* of each model. The *MEAN* of the training and test sets of XGB and GBR are both greater than one. RFR has the smallest *COV* in the training set, but the largest *COV* in the test set, indicating that its test set has the largest dispersion of prediction results, and the difference between the results of the RFR training set and test set is the largest, which is caused by its algorithm characteristics.

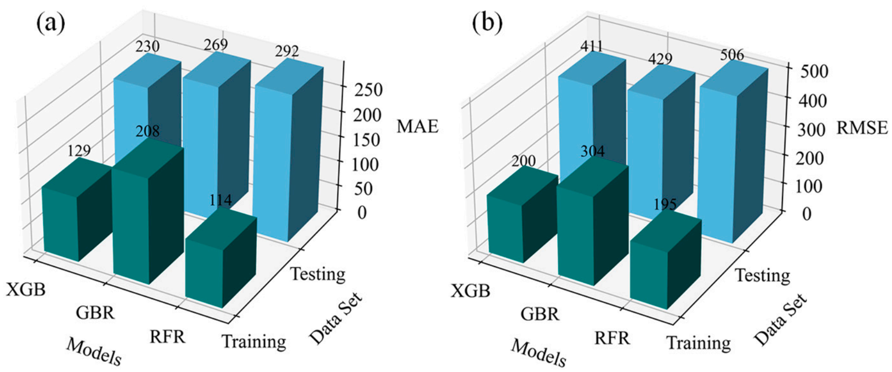

Figure 13. Mean absolute error and root mean square error of different models: (**a**) *MAE*; (**b**) *RMSE*.

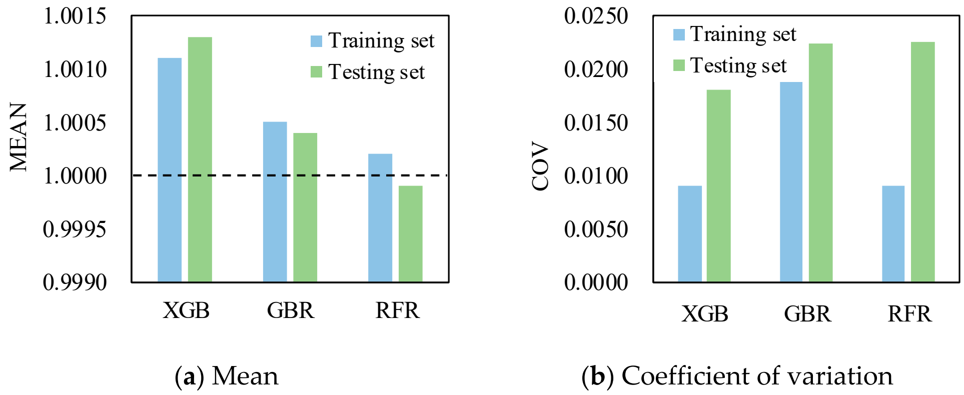

Figure 14. Mean and coefficient of variation of different models.

The errors between the prediction results and the true values of the training set and test set of the three models are counted, where error = $(N_u^{ML} - N_u^{FE})/N_u^{FE}$. The statistical results are shown in Table 5. It can be seen that overall, the prediction results of the three models are satisfactory. The error of the GBR training set, RFR training set, XGB training set, GBR testing set, RFR testing set, and XGB testing set are 2.4%, 0.1%, 0%, 2.7%, 3.5%, and 1.9%, respectively, and the proportion of errors exceeding 5% is less than 5%. In addition, it is worth noting that the results of the training set and test set of the XGB model show a significant difference: all the errors of the predicted values in the training set are within 0.5%, while about 65.8% of the predicted values in the test set have errors exceeding 0.5%.

Table 5. Predicted errors of different models.

ML Model		Percentage of Error (%)			
		≤0.5%	**0.5%~1%**	**1%~5%**	**≥5%**
GBR	Training set	28.2	21.9	47.6	2.4
	Testing set	20.8	18.3	58.1	2.7
RFR	Training set	55.3	24.7	19.9	0.1
	Testing set	24.0	18.5	54.0	3.5
XGB	Training set	100	0	0	0
	Testing set	34.2	21.7	42.3	1.9

4. Comparison with Existing Calculation Methods

The three trained predictive models featured in this study can be employed to swiftly predict the axial load-bearing capacity of new RECFST members. These models can quickly generate results for RECFST members in seconds, offering a significant advantage over finite element models that may require dozens of minutes or more for each load-bearing capacity calculation.

In this study, 60 RECFST specimens from existing references [7,10,21,78–83] have been collected along with their axial load test results. The axial load-bearing capacity for these specimens is determined through three machine learning-based predictive models. Predictions from these models were then compared with actual experimental outcomes, as collated in Table 6. In the table, N_u is the test result, and N_u^{RFR}, N_u^{XGB}, and N_u^{GBR} are the results predicted, respectively, by the RFR model, XGB model, and GBR model.

Table 6. Comparison between test results and results of prediction models.

Ref.	Specimens	N_u (kN)	N_u^{RFR} (kN)	$\frac{N_u^{RFR}}{N_u}$	N_u^{XGB} (kN)	$\frac{N_u^{XGB}}{N_u}$	N_u^{GBR} (kN)	$\frac{N_u^{GBR}}{N_u}$
[10]	WST1-A	3429	3326	0.97	3182	0.93	3327	0.97
	WST1-B	3338	3326	1.00	3182	0.95	3327	1.00
	WST2-A	4162	3790	0.91	3549	0.85	3570	0.86
	WST2-B	4168	3760	0.90	3537	0.85	3570	0.86
	WST3-A	3929	3712	0.94	3586	0.91	3701	0.94
	WST3-B	4158	3686	0.89	3729	0.90	3960	0.95
	WST4-A	4492	4381	0.98	4361	0.97	4405	0.98
	WST4-B	5530	5013	0.91	5031	0.91	5048	0.91
	WST5-A	5620	5431	0.97	5158	0.92	5506	0.98
	WST5-B	5500	5484	1.00	5158	0.94	5629	1.02
	WST6-A	3240	3655	1.13	3341	1.03	3618	1.12
	WST6-B	2993	3655	1.22	3332	1.11	3681	1.23
	WST7-A	4826	5437	1.13	5457	1.13	5305	1.10
	WST7-B	4944	5437	1.10	5457	1.10	5305	1.07
	WST8-A	6521	6873	1.05	6345	0.97	6478	0.99
	WST8-B	6493	6838	1.05	6229	0.96	6478	1.00
	WST9-A	4203	4709	1.12	4832	1.15	4829	1.15
	WST9-B	4180	4705	1.13	4846	1.16	4892	1.17
	WST10-A	7201	6847	0.95	6484	0.90	7165	1.00
	WST10-B	6905	6465	0.94	6483	0.94	6120	0.89
	WST11-A	9065	8730	0.96	8160	0.90	9338	1.03
	WST11-B	8799	8851	1.01	9219	1.05	9338	1.06
[78]	CFRT1-A	3429	3326	0.97	3182	0.93	3327	0.97
	CFRT1-B	3338	3326	1.00	3182	0.95	3327	1.00
	CFRT2-A	4162	3790	0.91	3549	0.85	3570	0.86
	CFRT2-B	4168	3760	0.90	3549	0.85	3570	0.86
	CFRT3-A	3929	3712	0.94	3556	0.91	3701	0.94
	CFRT3-B	4158	3724	0.90	3556	0.86	3901	0.94
	CFRT4-A	4492	4434	0.99	4361	0.97	4345	0.97
	CFRT4-B	5530	5013	0.91	5031	0.91	5048	0.91
	CFRT5-A	5620	5431	0.97	5158	0.92	5629	1.00
	CFRT5-B	5500	5484	1.00	5158	0.94	5629	1.02
[79]	C1	1339	1256	0.94	1251	0.93	1158	0.86
	C2	1444	1465	1.01	1493	1.03	1372	0.95
	C3	1755	1814	1.03	1787	1.02	1756	1.00
	C4	1825	1822	1.00	1748	0.96	1840	1.01
	C5	2125	2187	1.03	2190	1.03	2285	1.08
	C6	2319	2904	1.25	2696	1.16	2976	1.28
	C7	1623	1655	1.02	1618	1.00	1610	0.99
	C8	1954	2145	1.10	2158	1.10	2043	1.05
[80]	RCFST-A-0	2094	2118	1.01	2028	0.97	1948	0.93
[7]	RCFST-1	925	1047	1.13	947	1.02	1026	1.11
	RCFST-2	1215	1153	0.95	1357	1.12	1127	0.93
	RCFST-3	1635	1902	1.16	1917	1.17	2047	1.25
	RCFST-4	1658	1696	1.02	1566	0.94	1778	1.07
	RCFST-5	2091	2342	1.12	2009	0.96	2231	1.07

Table 6. *Cont.*

Ref.	Specimens	N_u (kN)	N_u^{RFR} (kN)	$\frac{N_u^{RFR}}{N_u}$	N_u^{XGB} (kN)	$\frac{N_u^{XGB}}{N_u}$	N_u^{GBR} (kN)	$\frac{N_u^{GBR}}{N_u}$
[21]	RR-1-180-4	1755	1826	1.04	1885	1.07	1756	1.00
	RR-1-180-6	2319	2630	1.13	2608	1.12	2618	1.13
	RR-0.5-180-6	1954	1997	1.02	2017	1.03	2038	1.04
	RR-0.5-180-4	1623	1465	0.90	1493	0.92	1372	0.85
[81]	RRCFST-A-180-1	2026	2214	1.09	2338	1.15	2250	1.11
	RRCFST-A-180-2	1915	2214	1.16	2334	1.22	2316	1.21
	RRCFST-C-180-1	1574	1655	1.05	1761	1.12	1704	1.08
[82]	PY1-180-e0-fy235	1780	1720	0.97	1735	0.97	1736	0.98
	PY1-180-fy345	2100	1928	0.92	2076	0.99	2036	0.97
	PYRE1-180-fy345	2060	1928	0.94	2076	1.01	2036	0.99
[83]	RCC1-4-180	1755	1814	1.03	1729	0.99	1756	1.00
	RCC1-6-180	2319	2523	1.09	2529	1.09	2503	1.08
	RCC0.5-4-180	1623	1459	0.90	1251	0.77	1351	0.83
	RCC0.5-6-180	1954	1904	0.97	1823	0.93	1865	0.95
	Mean			1.01		0.99		1.01
	Standard deviation			0.09		0.10		0.10

In this study, six theoretical methods are employed to calculate the axial compression-bearing capacity of RECFST, including formulas proposed by Ding et al. [10], Ren et al. [21], and Hassanein et al. [22], as well as formulas specified in different national standards (ACI 318-11 [72], GB 50936-2014 [73], and AISC 360-16 [74]), totaling from Equations (20)–(28). These methods are utilized to predict the axial load-bearing capacity of the aforementioned 60 RECSFT specimens, and their predictive performance is compared with that of three machine learning models used in this study. The predicted results from theoretical formulas and standard formulas are, respectively, presented in Tables A1 and A2.

(1) Ding's formula

Ding et al. [10] conducted a series of tests and FE studies on the RECFST under compression, and proposed a formula to calculate the compression-bearing capacity considering the difference in the strong and weak confinement regions of the core concrete, as shown in Equation (20).

$$N_u^{Ding} = A_c f_c[1 + (0.8 + 0.9K)\Phi] \tag{20}$$

where K is the sectional factor and Φ is the confinement factor, with details reported in Ref. [10].

(2) Ren's formula

$$N_u^{Ren} = f_c' A_c[1 + (1.75 - 0.691\kappa + 0.795\theta - 0.263\theta^2)\Phi] \tag{21}$$

where Φ is the confinement factor, κ is the aspect ratio of the middle rectangular part, and θ is central angle of the round ends, with details reported in Ref. [21].

(3) M.F. Hassanein's formula

$$N_u^{Hassanein} = \gamma_s f_y A_{s,RE} + \left(\gamma_c f_c' + 4.1 f_{rp}'\right) A_{c,RE} + f_y A_{s,RP,eff} + \gamma_c f_c' A_{c,RP} \tag{22}$$

where $A_{s,RE}$ and $A_{c,RE}$ are, respectively, the cross-sectional areas of the steel tube and the concrete in the round ends of the columns, while $A_{s,RP,eff}$ is the effective cross-sectional area of the steel in the rectangular part of the column, and $A_{c,RP}$ is the cross-sectional area of the concrete in the middle rectangular parts. γ_s is used to account for the effects of strain hardening and D/t ratio on the yield stress of the steels of circular tubes. The detailed information can be found in Ref. [22].

(4) Formula of code ACI 318-11

$$N_u^{ACI} = A_s f_y + 0.85 A_c f_c' \tag{23}$$

(5) Formula of code AISC 360-16

$$N_u^{AISC} = A_s f_y + C_2 A_c f_c' \tag{24}$$

where $C_2 = \begin{cases} 0.95 \text{ for circular cross- sec tion} \\ 0.85 \text{ for rectangular cross- sec tion} \end{cases}$

(6) Formula of code GB 50936-2014

$$N_u^{GB} = A_{sc} f_{sc} \tag{25}$$

$$f_{sc} = \left(1.212 + B\Phi + C\Phi^2\right) f_c \tag{26}$$

$$\Phi = \alpha_{sc} \frac{f_y}{f_c} \tag{27}$$

$$\alpha_{sc} = \frac{A_s}{A_c} \tag{28}$$

where B and C are the influence coefficient of cross-section shape on confinement effect; the specific values are referenced in Ref. [73].

Figures 15 and 16 display the ratio of the predicted values to the tested values for each calculation model. The mean ratios of the predicted to tested values for the RFR, XGB, and GBR machine learning models are 1.01, 0.99, and 1.01, respectively. The corresponding standard deviations are 0.09, 0.10, and 0.10. Meanwhile, the mean ratios of the bearing capacity values calculated by Ding's, Ren's, and Hassanein's empirical formulas and the ACI, GB, and AISC standard formulas to the tested values are 1.07, 0.94, 1.02, 0.88, 1.09, and 0.90, respectively. Their corresponding standard deviations are 0.10, 0.13, 0.12, 0.08, 0.08, and 0.07, respectively.

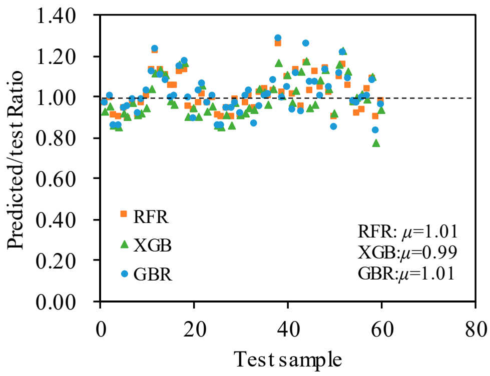

Figure 15. Ratios of the values predicted by the machine learning models to the tested values.

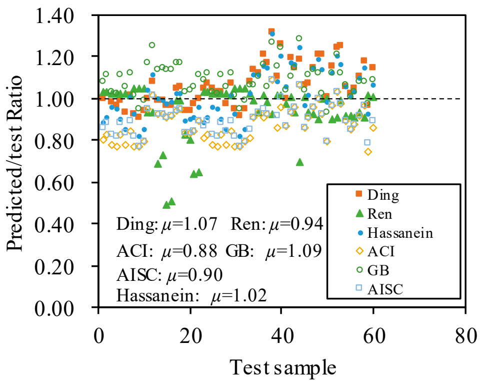

Figure 16. Ratios of the values predicted by the existing methods to the tested values.

The errors between the tested values and the calculation results of various calculation methods are counted, where error = $(N_u^{Pre} - N_u)/N_u$, as shown in Figure 17. It can be seen that the calculation results of the ACI and AISC codes are conservative, and the percentage of specimens where the predicted values are lower than the tested values reached 93.55% and 91.94%, respectively. The observed conservatism in the calculation results of the ACI and AISC standards could be attributed to the fact that these two standards have uniformly reduced the bearing capacity of the concrete. Contrarily, the GB standard tends to overestimate the load-bearing capacity, with the rate of specimens having predicted values exceeding the measured values reaching 88.71%.

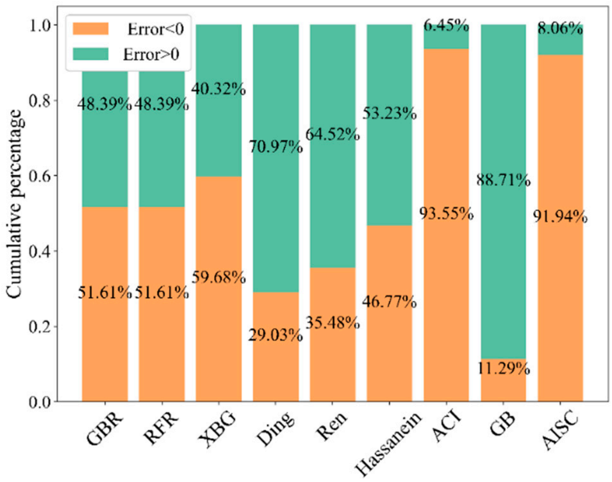

Figure 17. Proportion of Error < 0 and Error > 0 of different methods.

Among the above calculation methods, the GBR model, RFR model, and XGB model in machine learning achieved better prediction results, as shown in Figure 18. The proportion of predictions with an error less than 5% (0 < Error < 5% or 0 > Error > −5%) are 43.55%, 40.32%, and 33.87%, respectively, which are significantly higher than the rest of the theoretical models or standard formulas. The proportions of predictions where the error exceeds 15% (Error < −15% or Error > 15%) are only 14.52%, 9.68%, and 14.52%, respectively. These results show that the predictions made using the above three calculation methods for the axial compression-bearing capacity of RECFST are satisfactory.

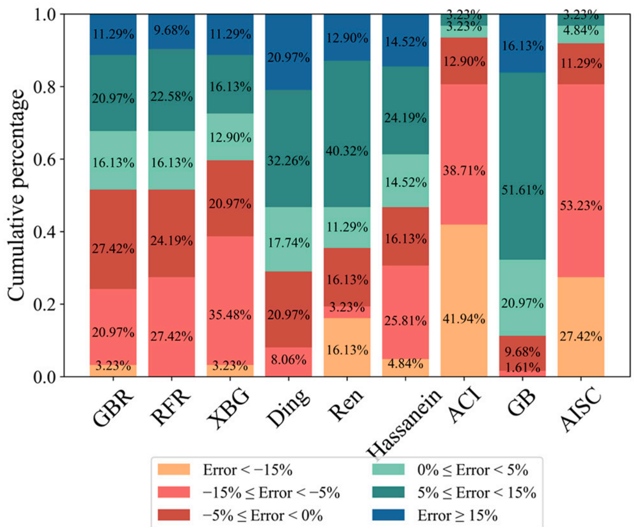

Figure 18. Proportion of errors of different methods.

Based on the Python platform, these three pre-trained prediction models are integrated into a graphics user-friendly interactive interface (GUI), as illustrated in Figure 19. Within this GUI, the key parameters of the round-ended steel tube concrete, namely B, D, t, f_{cu}, and f_y, can be directly inputted. By simply clicking the calculate button, the axial load-bearing capacities as forecasted by the three models can be instantly displayed. This method proves to be highly accurate compared to the existing theoretical formulas and standards, and, in comparison to finite element models, offers a significant advantage in computational efficiency. Thus, it is highly meaningful for the rapid design of RECFST components.

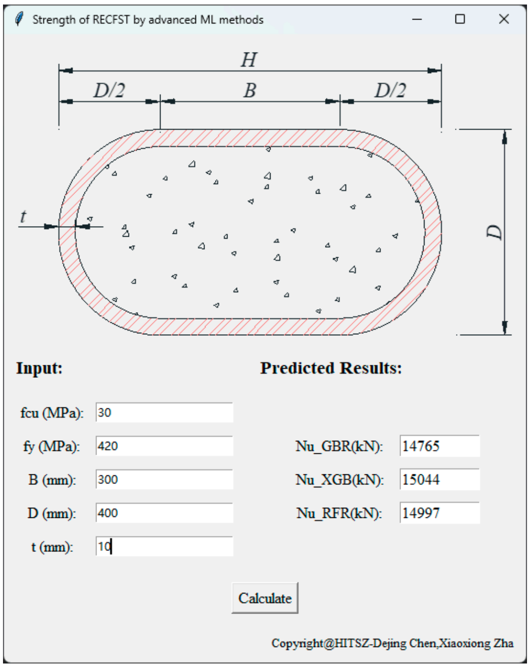

Figure 19. GUI for calculation of compression capacity of RECFST by advanced ML methods.

5. Conclusions

The present study employs advanced machine learning methods, namely GBR (Gradient Boosting Regressor), RFR (Random Forest Regressor), and XGB (Extreme Gradient Boosting), to predict the axial load-bearing capacity of round-ended concrete-filled steel tube (RECFST). These methods are characterized by high computational efficiency, a wide range of parameters, and high accuracy, playing an important role in the design of RECFST. The following conclusions are drawn:

(1) Using the finite element method, a machine learning database comprising 2400 RECFSTs is established. This database encompasses commonly used material strengths and cross-sectional dimensions of RECFST, effectively addressing the issue of insufficient experimental sample size in the current machine learning practices.

(2) Through sensitive analysis, in addition to the primary parameter, the second parameters such as $A_c f_{cu}$, $A_c + A_s$, A_c, A_s, and $A_s f_y$ also show a large correlation with the axial load-bearing capacity N_u, with their Pearson coefficients being 0.968, 0.909, 0.904, 0.694, and 0.684, respectively. Identifying these fundamental parameters closely related to axial load-bearing capacity is an essential foundation for applying machine learning to predict load-bearing capacity.

(3) The three predictive models for the axial load-bearing capacity of RECFST, utilizing advanced machine learning methods, demonstrate higher accuracy compared to the existing theoretical or code-based calculation formulas. Furthermore, they exhibit higher efficiency compared to finite element methods. The development of a graphical user interface (GUI) based on these machine learning prediction models enables the

rapid and accurate prediction of the axial load-bearing capacity of RECFST. This development holds significant importance for the engineering applications of RECFST.

In this paper, only the axial compression performance of RECFST stub columns was considered. In future studies, more attention should be paid to the influence of important parameters such as slenderness ratio on the axial compression performance of RECFST members. In addition, machine learning methods also have great potential in predicting the bending, shear, or torsion resistance of RECFST members. In the future, the author plans to pursue related research.

Author Contributions: Conceptualization, D.C. and X.Z.; methodology, D.C. and Y.F.; software, D.C.; validation, D.C. and Y.F.; writing—original draft preparation, D.C.; writing—review and editing, D.C.; visualization, D.C.; supervision, X.Z.; project administration, X.Z.; funding acquisition, X.Z. and D.C. All authors have read and agreed to the published version of the manuscript.

Funding: This research was funded by the National Natural Science Foundation of China, grant numbers 52178129 and 52408167.

Data Availability Statement: The original contributions presented in the study are included in the article, further inquiries can be directed to the corresponding author.

Conflicts of Interest: The authors declare that they have no conflicts of interest in this work.

Appendix A

Table A1. Comparison between test results and results of theoretical formulas.

Ref.	Specimens	N_u (kN)	N_u^{Ding} (kN)	$\frac{N_u^{Ding}}{N_u}$	N_u^{Ren} (kN)	$\frac{N_u^{Ren}}{N_u}$	$N_u^{Hassanein}$ (kN)	$\frac{N_u^{Hassanein}}{N_u}$
[10]	WST1-A	3429	3436	1.00	3695	1.03	3032	0.88
	WST1-B	3338	3419	1.02	3685	1.03	3040	0.91
	WST2-A	4162	4101	0.99	4469	1.03	3996	0.96
	WST2-B	4168	4046	0.97	4403	1.03	3955	0.95
	WST3-A	3929	3881	0.99	4157	1.02	3529	0.90
	WST3-B	4158	3879	0.93	4140	1.02	3530	0.85
	WST4-A	4492	4548	1.01	4891	1.02	4543	1.01
	WST4-B	5530	5127	0.93	5542	1.05	5114	0.92
	WST5-A	5620	5107	0.91	5377	1.05	4630	0.82
	WST5-B	5500	5196	0.94	5479	1.05	4699	0.85
	WST6-A	3240	3247	1.00	3376	0.93	3374	1.04
	WST6-B	2993	3237	1.08	3334	0.93	3330	1.11
	WST7-A	4826	4776	0.99	3426	0.69	4809	1.00
	WST7-B	4944	4913	0.99	3721	0.73	4915	0.99
	WST8-A	6521	6282	0.96	3216	0.50	6381	0.98
	WST8-B	6493	6275	0.97	3292	0.51	6367	0.98
	WST9-A	4203	4423	1.05	4468	0.99	4314	1.03
	WST9-B	4180	4405	1.05	4452	0.99	4296	1.03
	WST10-A	7201	6758	0.94	5402	0.83	6442	0.89
	WST10-B	6905	6513	0.94	5076	0.81	6241	0.90
	WST11-A	9065	8853	0.98	5263	0.64	8237	0.91
	WST11-B	8799	8761	1.00	5489	0.65	8420	0.96
[78]	CFRT1-A	3429	3603	1.05	3709	1.03	3043	0.89
	CFRT1-B	3338	3586	1.07	3690	1.03	3046	0.91
	CFRT2-A	4162	4351	1.05	4472	1.03	4000	0.96
	CFRT2-B	4168	4293	1.03	4411	1.03	3964	0.95
	CFRT3-A	3929	4069	1.04	4158	1.02	3530	0.90
	CFRT3-B	4158	4066	0.98	4149	1.02	3537	0.85
	CFRT4-A	4492	4825	1.07	4899	1.02	4548	1.01
	CFRT4-B	5530	5272	0.95	5543	1.05	5115	0.92
	CFRT5-A	5620	5137	0.91	5378	1.05	4631	0.82
	CFRT5-B	5500	5225	0.95	5479	1.05	4699	0.85

Table A1. *Cont.*

Ref.	Specimens	N_u (kN)	N_u^{Ding} (kN)	$\frac{N_u^{Ding}}{N_u}$	N_u^{Ren} (kN)	$\frac{N_u^{Ren}}{N_u}$	$N_u^{Hassanein}$ (kN)	$\frac{N_u^{Hassanein}}{N_u}$
[79]	C1	1339	1445	1.08	1476	1.02	1367	1.02
	C2	1444	1647	1.14	1638	0.99	1606	1.11
	C3	1755	1968	1.12	1845	0.94	1961	1.12
	C4	1825	2218	1.22	2253	1.02	2100	1.15
	C5	2125	2495	1.17	2463	0.99	2429	1.14
	C6	2319	3056	1.32	2833	0.93	3046	1.31
	C7	1623	1789	1.10	1820	1.02	1754	1.08
	C8	1954	2471	1.26	2501	1.01	2357	1.21
[80]	RCFST-A-0	2094	2092	1.00	2037	0.97	2213	1.06
[7]	RCFST-1	925	1108	1.20	1116	1.01	1084	1.17
	RCFST-2	1215	1391	1.14	1296	0.93	1410	1.16
	RCFST-3	1635	1943	1.19	1353	0.70	2034	1.24
	RCFST-4	1658	1768	1.07	1776	1.00	1604	0.97
	RCFST-5	2091	2243	1.07	2104	0.94	2116	1.01
[21]	RR-1-180-4	1755	2012	1.15	1865	0.93	2010	1.15
	RR-1-180-6	2319	2805	1.21	2538	0.90	2754	1.19
	RR-0.5-180-6	1954	2361	1.21	2354	1.00	2219	1.14
	RR-0.5-180-4	1623	1641	1.01	1647	1.00	1589	0.98
[81]	RRCFST-A-180-1	2026	2345	1.16	2106	0.90	2277	1.12
	RRCFST-A-180-2	1915	2389	1.25	2178	0.91	2308	1.21
	RRCFST-C-180-1	1574	1975	1.25	1965	1.00	1830	1.16
[82]	PY1-180-e0-fy235	1780	1879	1.06	1730	0.92	1881	1.06
	PY1-180-fy345	2100	2150	1.02	1969	0.92	2108	1.00
	PYRE1-180-fy345	2060	2166	1.05	1974	0.91	2126	1.03
[83]	RCC1-4-180	1755	1937	1.10	1813	0.94	1925	1.10
	RCC1-6-180	2319	2729	1.18	2493	0.91	2664	1.15
	RCC0.5-4-180	1623	1569	0.97	1591	1.01	1497	0.92
	RCC0.5-6-180	1954	2247	1.15	2267	1.01	2075	1.06
	Mean			1.06		0.94		1.02
	Standard deviation			0.10		0.13		0.12

Table A2. Comparison between test results and results of existing standards.

Ref.	Specimens	N_u (kN)	N_u^{ACI} (kN)	$\frac{N_u^{ACI}}{N_u}$	N_u^{GB} (kN)	$\frac{N_u^{GB}}{N_u}$	N_u^{AISC} (kN)	$\frac{N_u^{AISC}}{N_u}$
[10]	WST1-A	3429	2763	0.81	3719	1.08	2960	0.86
	WST1-B	3338	2771	0.83	3730	1.12	2968	0.89
	WST2-A	4162	3245	0.78	4305	1.03	3444	0.83
	WST2-B	4168	3216	0.77	4266	1.02	3413	0.82
	WST3-A	3929	3251	0.83	4387	1.12	3491	0.89
	WST3-B	4158	3249	0.78	4383	1.05	3488	0.84
	WST4-A	4492	3780	0.84	5029	1.12	4019	0.89
	WST4-B	5530	4253	0.77	5605	1.01	4548	0.82
	WST5-A	5620	4323	0.77	5347	0.95	4323	0.77
	WST5-B	5500	4393	0.80	5436	0.99	4393	0.80
	WST6-A	3240	3093	0.95	3805	1.17	3093	0.95
	WST6-B	2993	3051	1.02	3754	1.25	3051	1.02
	WST7-A	4826	4454	0.92	5509	1.14	4454	0.92
	WST7-B	4944	4563	0.92	5654	1.14	4563	0.92
	WST8-A	6521	5957	0.91	7408	1.14	5957	0.91
	WST8-B	6493	5945	0.92	7405	1.14	5945	0.92
	WST9-A	4203	3975	0.95	4921	1.17	3975	0.95
	WST9-B	4180	3959	0.95	4905	1.17	3959	0.95

Table A2. *Cont.*

Ref.	Specimens	N_u (kN)	N_u^{ACI} (kN)	$\frac{N_u^{ACI}}{N_u}$	N_u^{GB} (kN)	$\frac{N_u^{GB}}{N_u}$	N_u^{AISC} (kN)	$\frac{N_u^{AISC}}{N_u}$
[10]	WST10-A	7201	5997	0.83	7460	1.04	5997	0.83
	WST10-B	6905	5793	0.84	7199	1.04	5793	0.84
	WST11-A	9065	7688	0.85	9593	1.06	7688	0.85
	WST11-B	8799	7873	0.89	9816	1.12	7873	0.89
[78]	CFRT1-A	3429	2774	0.81	3735	1.09	2972	0.87
	CFRT1-B	3338	2776	0.83	3737	1.12	2974	0.89
	CFRT2-A	4162	3248	0.78	4309	1.04	3447	0.83
	CFRT2-B	4168	3224	0.77	4278	1.03	3422	0.82
	CFRT3-A	3929	3252	0.83	4388	1.12	3492	0.89
	CFRT3-B	4158	3256	0.78	4393	1.06	3496	0.84
	CFRT4-A	4492	3785	0.84	5035	1.12	4024	0.90
	CFRT4-B	5530	4254	0.77	5606	1.01	4549	0.82
	CFRT5-A	5620	4324	0.77	5348	0.95	4324	0.77
	CFRT5-B	5500	4393	0.80	5436	0.99	4393	0.80
[79]	C1	1339	1086	0.81	1422	1.06	1146	0.86
	C2	1444	1310	0.91	1538	1.06	1310	0.91
	C3	1755	1641	0.94	1944	1.11	1641	0.94
	C4	1825	1654	0.91	2127	1.17	1733	0.95
	C5	2125	1960	0.92	2245	1.06	1960	0.92
	C6	2319	2526	1.09	2936	1.27	2526	1.09
	C7	1623	1402	0.86	1868	1.15	1493	0.92
	C8	1954	1873	0.96	2425	1.24	1966	1.01
[80]	RCFST-A-0	2094	1816	0.87	2171	1.04	1816	0.87
[7]	RCFST-1	925	866	0.94	1022	1.10	866	0.94
	RCFST-2	1215	1164	0.96	1392	1.15	1164	0.96
	RCFST-3	1635	1739	1.06	2100	1.28	1739	1.06
	RCFST-4	1658	1422	0.86	1729	1.04	1422	0.86
	RCFST-5	2091	1903	0.91	2335	1.12	1903	0.91
[21]	RR-1-180-4	1755	1688	0.96	2001	1.14	1688	0.96
	RR-1-180-6	2319	2315	1.00	2609	1.13	2315	1.00
	RR-0.5-180-6	1954	1804	0.92	2008	1.03	1804	0.92
	RR-0.5-180-4	1623	1292	0.80	1516	0.93	1292	0.80
[81]	RRCFST-A-180-1	2026	1956	0.97	2281	1.13	1956	0.97
	RRCFST-A-180-2	1915	1983	1.04	2316	1.21	1983	1.04
	RRCFST-C-180-1	1574	1532	0.97	1767	1.12	1532	0.97
[82]	PY1-180-e0-fy235	1780	1586	0.89	1896	1.07	1586	0.89
	PY1-180-fy345	2100	1796	0.86	2110	1.00	1796	0.86
	PYRE1-180-fy345	2060	1813	0.88	2131	1.03	1813	0.88
[83]	RCC1-4-180	1755	1614	0.92	1904	1.08	1614	0.92
	RCC1-6-180	2319	2237	0.96	2510	1.08	2237	0.96
	RCC0.5-4-180	1623	1208	0.74	1584	0.98	1276	0.79
	RCC0.5-6-180	1954	1674	0.86	2134	1.09	1744	0.89
	Mean			0.88		1.09		0.90
	Standard deviation			0.08		0.08		0.07

References

1. Long, Y.-L.; Zeng, L. A refined model for local buckling of rectangular CFST columns with binding bars. *Thin Walled Struct.* **2018**, *132*, 431–441. [CrossRef]
2. Long, Y.-L.; Wan, J.; Cai, J. Theoretical study on local buckling of rectangular CFT columns under eccentric compression. *J. Constr. Steel Res.* **2016**, *120*, 70–80. [CrossRef]
3. Wang, Q.-K.; Chen, M.; Lu, Z.-A. Finite element analysis for the mechanical behaviors of circle-ended concrete-filled steel tubular tower. In Proceedings of the 2009 Second International Conference on Information and Computing Science, Manchester, UK, 21–22 May 2009; pp. 110–113.

4. Xie, J.X.; Lu, Z.A.; Tang, P.; Liu, D. Modal Analysis and Experimental Study on Round-Ended CFST Coupled Column Cable Stayed Bridge. In Proceedings of the 2011 Second International Conference on Mechanic Automation and Control Engineering, Inner Mongolia, China, 15–17 July 2011; pp. 2302–2304.
5. Xie, J.-X.; Lu, Z.-A. Numerical Simulation and Test Study on Non-Uniform Area of Round-Ended CFST Tubular Tower. In Proceedings of the 2010 Third International Conference on Information and Computing, Wuxi, China, 4–6 June 2010; pp. 19–22.
6. Xie, J.X.; Lu, Z.A. Test Study and Contact Analysis of Round-Ended CFST Coupled Column. In Proceedings of the 2nd International Conference on Model and Simulation, Rome, Italy, 2–6 March 2009. pp. 28–32.
7. Wang, Z.B.; Chen, J.; Xie, E.P.; Lin, S. Behavior of concrete-filled round-end steel tubular stubcolumns under axial compression. *J. Build. Structures* **2014**, *35*, 123–130. (In Chinese)
8. Guo, J.-T.; Wang, Z.-B.; Tan, E.L.; Gao, Y.-H. Flexural performance of round-ended concrete-filled steel tubular specimens. *J. Constr. Steel Res.* **2024**, *215*, 108529. [CrossRef]
9. Ding, F.X.; Zhang, T.; Wang, L.; Fu, L. Further analysis on the flexural behavior of concrete-filled round-ended steel tubes. *Steel Compos. Struct.* **2019**, *30*, 149–169.
10. Faxing, D.; Lei, F.; Zhiwu, Y.; Gang, L. Mechanical performances of concrete-filled steel tubular stub columns with round ends under axial loading. *Thin-Walled Struct.* **2015**, *97*, 22–34. [CrossRef]
11. Ding, F.; Xiong, S.; Zhang, H.; Li, G.; Zhao, P.; Xiang, P. Reliability analysis of axial bearing capacity of concrete filled steel tubular stub columns with different cross sections. *Structures* **2021**, *33*, 4193–4202. [CrossRef]
12. Shen, Q.; Wang, F.; Wang, J.; Ma, X. Cyclic behaviour and design of cold-formed round-ended concrete-filled steel tube columns. *J. Constr. Steel Res.* **2022**, *190*, 107089. [CrossRef]
13. Shen, Q.; Wang, J.; Liew, J.R.; Gao, B.; Xiao, Q. Experimental study and strength evaluation of axially loaded welded tubular joints with round-ended oval hollow sections. *Thin-Walled Struct.* **2020**, *154*, 106846. [CrossRef]
14. Wang, J.; Shen, Q. Numerical analysis and design of thin-walled RECFST stub columns under axial compression. *Thin-Walled Struct.* **2018**, *129*, 166–182. [CrossRef]
15. Shen, Q.H.; Wang, J.F.; Wang, W.Q.; Wang, Z.B. Performance and design of eccentrically-loaded concrete-filled round-ended elliptical hollow section stub columns. *J. Constr. Steel Res.* **2018**, *150*, 99–114. [CrossRef]
16. Xing, W.B.; Shen, Q.H.; Wang, J.F.; Sheng, M.Y. Performance and design of oval-ended elliptical CFT columns under combined axial compression-torsion. *J. Constr. Steel Res.* **2020**, *172*, 106148. [CrossRef]
17. Wang, R.; Li, X.; Zhao, H.; Wang, Y.H.; Lam, D.; Chen, M.T. Eccentric compression performance of round-ended CFST slender columns with different aspect ratios. *J. Constr. Steel Res.* **2023**, *211*, 108198. [CrossRef]
18. Zhao, H.; Mei, S.Q.; Wang, R.; Yang, X.; Lam, D.; Chen, W.S. Round-ended concrete-filled steel tube columns under impact loading: Test, numerical analysis and design method. *Thin-Walled Struct.* **2023**, *191*, 111020. [CrossRef]
19. Zhao, H.; Mei, S.Q.; Wang, R.; Yang, X.; Wang, W.D.; Chen, W.S. Performance of round-ended CFST columns under combined actions of eccentric compression and impact loads. *Eng. Struct.* **2024**, *301*, 117328. [CrossRef]
20. Zhao, H.; Zhang, W.H.; Wang, R.; Hou, C.C.; Lam, D. Axial compression behaviour of round-ended recycled aggregate concrete-filled steel tube stub columns (RE-RACFST): Experiment, numerical modeling and design. *Eng. Struct.* **2023**, *276*, 115376. [CrossRef]
21. Ren, Z.G.; Wang, D.D.; Li, P.P. Axial compressive behaviour and confinement effect of round-ended rectangular CFST with different central angles. *Compos. Struct.* **2022**, *285*, 115193. [CrossRef]
22. Hassanein, M.F.; Patel, V.I. Round-ended rectangular concrete-filled steel tubular short columns: FE investigation under axial compression. *J. Constr. Steel Res.* **2018**, *140*, 222–236. [CrossRef]
23. Piquer, A.; Ibañez, C.; Hernández-Figueirido, D. Structural response of concrete-filled round-ended stub columns subjected to eccentric loads. *Eng. Struct.* **2019**, *184*, 318–328. [CrossRef]
24. Patel, V.I. Analysis of uniaxially loaded short round-ended concrete-filled steel tubular beam-columns. *Eng. Struct.* **2020**, *205*, 110098. [CrossRef]
25. Zhang, Q.; Fu, L.; Xu, L. An efficient approach for numerical simulation of concrete-filled round-ended steel tubes. *J. Constr. Steel Res.* **2020**, *170*, 106086. [CrossRef]
26. Ahmed, M.; Liang, Q.Q. Numerical analysis of thin-walled round-ended concrete-filled steel tubular short columns including local buckling effects. *Structures* **2020**, *28*, 181–196. [CrossRef]
27. Ahmed, M.; Liang, Q.Q.; Patel, V.I.; Gohari, S.; Hamoda, A. Unified numerical model for performance analysis of various cross-sections of concrete-filled stainless-steel tubular stub columns under axial loading. *Structures* **2023**, *55*, 799–817. [CrossRef]
28. Jordan, M.I.; Mitchell, T.M. Machine learning: Trends, perspectives, and prospects. *Science* **2015**, *349*, 255–260. [CrossRef] [PubMed]
29. Yu, Y.; Liang, S.; Samali, B.; Nguyen, T.N.; Zhai, C.; Li, J.; Xie, X. Torsional capacity evaluation of RC beams using an improved bird swarm algorithm optimised 2D convolutional neural network. *Eng. Struct.* **2022**, *273*, 115066. [CrossRef]
30. Yu, Y.; Zhang, C.; Xie, X.; Yousefi, A.M.; Zhang, G.; Li, J.; Samali, B. Compressive strength evaluation of cement-based materials in sulphate environment using optimized deep learning technology. *Dev. Built. Environ.* **2023**, *16*, 100298. [CrossRef]
31. Güneyisi, E.M.; Gültekin, A.; Mermerdaş, K. Ultimate capacity prediction of axially loaded CFST short columns. *Int. J. Steel Struct.* **2016**, *16*, 99–114. [CrossRef]

32. Hou, C.; Zhou, X.G. Strength prediction of circular CFST columns through advanced machine learning methods. *J. Build. Eng.* **2022**, *51*, 104289. [CrossRef]
33. Ngo, N.-T.; Le, H.A.; Pham, T.-P. Integration of support vector regression and grey wolf optimization for estimating the ultimate bearing capacity in concrete-filled steel tube columns. *Neural Comput. Appl.* **2021**, *33*, 8525–8542. [CrossRef]
34. Nguyen, M.-S.T.; Trinh, M.-C.; Kim, S.-E. Uncertainty quantification of ultimate compressive strength of CCFST columns using hybrid machine learning model. *Eng. Comput.* **2022**, *38*, 2719–2738. [CrossRef]
35. Sarir, P.; Chen, J.; Asteris, P.G.; Armaghani, D.J.; Tahir, M.M. Developing GEP tree-based, neuro-swarm, and whale optimization models for evaluation of bearing capacity of concrete-filled steel tube columns. *Eng. Comput.* **2021**, *37*, 1–19. [CrossRef]
36. Sarir, P.; Shen, S.-L.; Wang, Z.-F.; Chen, J.; Horpibulsuk, S.; Pham, B.T. Optimum model for bearing capacity of concrete-steel columns with AI technology via incorporating the algorithms of IWO and ABC. *Eng. Comput.* **2021**, *37*, 797–807. [CrossRef]
37. Degtyarev, V.V.; Thai, H.T. Design of concrete-filled steel tubular columns using data-driven methods. *J. Constr. Steel Res.* **2023**, *200*, 107653. [CrossRef]
38. Duong, T.H.; Le, T.-T.; Le, M.V. Practical Machine Learning Application for Predicting Axial Capacity of Composite Concrete-Filled Steel Tube Columns Considering Effect of Cross-Sectional Shapes. *Int. J. Steel Struct.* **2023**, *23*, 263–278. [CrossRef]
39. Le, T.-T.; Phan, H.C. Prediction of Ultimate Load of Rectangular CFST Columns Using Interpretable Machine Learning Method. *Adv. Civ. Eng.* **2020**, *2020*, e8855069. [CrossRef]
40. Nguyen, T.-A.; Trinh, S.H.; Nguyen, M.H.; Ly, H.-B. Novel ensemble approach to predict the ultimate axial load of CFST columns with different cross-sections. *Structures* **2023**, *47*, 1–14. [CrossRef]
41. Nguyen, T.; Le Nguyen, K.; Ly, H. Universal boosting ML approaches to predict the ultimate load capacity of CFST columns. *Struct. Des. Tall Spec. Build.* **2024**, *33*, e2071. [CrossRef]
42. Tran, V.L.; Jang, Y.; Kim, S.E. Improving the axial compression capacity prediction of elliptical CFST columns using a hybrid ANN-IP model. *Steel Compos. Struct.* **2021**, *39*, 319–335.
43. Zarringol, M.; Thai, H.T. Prediction of the load-shortening curve of CFST columns using ANN-based models. *J. Build. Eng.* **2022**, *51*, 104279. [CrossRef]
44. Zhou, X.-G.; Hou, C.; Feng, W.-Q. Optimized data-driven machine learning models for axial strength prediction of rectangular CFST columns. *Structures* **2023**, *47*, 760–780. [CrossRef]
45. Zhou, X.-G.; Hou, C.; Peng, J. Active learning methods for strength assessment of circular CFST under coupled long-term axial loading and random localized corrosion. *Thin-Walled Struct.* **2023**, *193*, 111254. [CrossRef]
46. Hanoon, A.N.; Al Zand, A.W.; Yaseen, Z.M. Designing new hybrid artificial intelligence model for CFST beam flexural performance prediction. *Eng. Comput.* **2022**, *38*, 3109–3135. [CrossRef]
47. Hou, C.; Zhou, X.-G.; Shen, L. Intelligent prediction methods for N–M interaction of CFST under eccentric compression. *Arch. Civ. Mech. Eng.* **2023**, *23*, 197. [CrossRef]
48. Huang, H.; Xue, C.; Zhang, W.; Guo, M. Torsion design of CFRP-CFST columns using a data-driven optimization approach. *Eng. Struct.* **2022**, *251*, 113479. [CrossRef]
49. Wang, C.; Chan, T.M. Machine learning (ML) based models for predicting the ultimate strength of rectangular concrete-filled steel tube (CFST) columns under eccentric loading. *Eng. Struct.* **2023**, *276*, 115392. [CrossRef]
50. Zarringol, M.; Thai, H.-T.; Naser, M. Application of machine learning models for designing CFCFST columns. *J. Constr. Steel Res.* **2021**, *185*, 106856. [CrossRef]
51. Zarringol, M.; Patel, V.I.; Liang, Q.Q.; Hassanein, M.F.; Ahmed, M. Machine-learning-based predictive models for concrete-filled double skin tubular columns. *Eng. Struct.* **2024**, *304*, 117593. [CrossRef]
52. Hong, Z.-T.; Wang, W.-D.; Zheng, L.; Shi, Y.-L. Machine learning models for predicting axial compressive capacity of circular CFDST columns. *Structures* **2023**, *57*, 105285. [CrossRef]
53. Miao, K.; Pan, Z.; Chen, A.; Wei, Y.; Zhang, Y. Machine learning-based model for the ultimate strength of circular concrete-filled fiber-reinforced polymer–steel composite tube columns. *Constr. Build. Mater.* **2023**, *394*, 132134. [CrossRef]
54. Zarringol, M.; Patel, V.I.; Liang, Q.Q. Artificial neural network model for strength predictions of CFST columns strengthened with CFRP. *Eng. Struct.* **2023**, *281*, 115784. [CrossRef]
55. Chen, K.; Wang, S.; Wang, Y.; Wei, J.; Wang, Q.; Du, W.; Jin, W. Intelligent design of limit states for recycled aggregate concrete filled steel tubular columns. *Structures* **2023**, *58*, 105338. [CrossRef]
56. Zhou, X.-G.; Hou, C.; Peng, J.; Yao, G.-H.; Fang, Z. Structural mechanism-based intelligent capacity prediction methods for concrete-encased CFST columns. *J. Constr. Steel Res.* **2023**, *202*, 107769. [CrossRef]
57. Han, L.-H.; Yao, G.-H.; Tao, Z. Performance of concrete-filled thin-walled steel tubes under pure torsion. *Thin-Walled Struct.* **2007**, *45*, 24–36. [CrossRef]
58. Hillerborg, A.; Modéer, M.; Petersson, P.-E. Analysis of crack formation and crack growth in concrete by means of fracture mechanics and finite elements. *Cem. Concr. Res.* **1976**, *6*, 773–781. [CrossRef]
59. Jiang, J.J.; Lu, X.Z.; Ye, L.P. *Finite Element Analysis of Concrete Structures*; Beijing Tsinhhua University Press: Beijing, China, 2005. (In Chinese)
60. Shen, J.M.; Wang, C.Z.; Jiang, J.Q. *Finite Element Analysis of Reinforced Concrete and Limit Analysis of Plates and Shells*; Tsinhhua University Press: Beijing, China, 1993. (In Chinese)

61. Hu, H.-T.; Huang, C.-S.; Wu, M.-H.; Wu, Y.-M. Nonlinear analysis of axially loaded concrete-filled tube columns with confinement effect. *J. Struct. Eng.* **2003**, *129*, 1322–1329. [CrossRef]
62. Lin, S.; Zhao, Y.-G. Numerical study of the behaviors of axially loaded large-diameter CFT stub columns. *J. Constr. Steel Res.* **2019**, *160*, 54–66. [CrossRef]
63. Guo, L.; Zhang, S.; Kim, W.-J.; Ranzi, G. Behavior of square hollow steel tubes and steel tubes filled with concrete. *Thin-Walled Struct.* **2007**, *45*, 961–973. [CrossRef]
64. Nassiraei, H. Probabilistic Analysis of Strength in Retrofitted X-Joints under Tensile Loading and Fire Conditions. *Buildings* **2024**, *14*, 2105. [CrossRef]
65. Yu, M. Research on the Consecutive Theory of Concrete-Filled Steel Members Under Normal to High Temperature and Impact Load. Ph.D. Thesis, Harbin Institute of Technology, Harbin, China, 2011. (In Chinese)
66. Han, L.-H.; Li, W.; Bjorhovde, R. Developments and advanced applications of concrete-filled steel tubular (CFST) structures: Members. *J. Constr. Steel Res.* **2014**, *100*, 211–228. [CrossRef]
67. Evirgen, B.; Tuncan, A.; Taskin, K. Structural behavior of concrete filled steel tubular sections (CFT/CFSt) under axial compression. *Thin-Walled Struct.* **2014**, *80*, 46–56. [CrossRef]
68. *GB50017-2017*; Standard for Design of Steel Structures. China Architecture & Building Press: Beijing, China, 2017. (In Chinese)
69. *GB 50010-2010*; Code for Design of Concrete Structures. China Architecture & Building Press: Beijing, China, 2015. (In Chinese)
70. Chen, D.; Zha, X.; Fan, Y. Theoretical and experimental investigations on the stability performance of concrete-filled steel tubular X-column with regard to the flexural rigidity variation. *J. Build. Eng.* **2023**, *78*, 107698. [CrossRef]
71. Pearson, K., VII. Note on regression and inheritance in the case of two parents. *Proc. R. Soc. Lond.* **1895**, *58*, 240–242.
72. *ACI 318-11*; Building Code Requirements for Structural Concrete and Commentary. American Concrete Institute: Farmington Hills, MI, USA, 2011.
73. *GB 50936-2014*; Technical Code for Concrete Filled Steel Tubular Structures. China Architecture & Building Press: Beijing, China, 2014. (In Chinese)
74. *ANSI/AISC 360-16*; Specification for Structural Steel Buildings. American Institute of Steel Construction: Chicago, IL, USA, 2016.
75. Friedman, J.H. Greedy function approximation: A gradient boosting machine. *Ann. Stat.* **2001**, *29*, 1189–1232. [CrossRef]
76. Chen, T.Q.; Guestrin, C. XGBoost: A Scalable Tree Boosting System. In Proceedings of the 22nd ACM SIGKDD International Conference on Knowledge Discovery and Data Mining, San Francisco, CA, USA, 13–17 August 2016; Association for Computing Machinery: New York, NY, USA, 2016; pp. 785–794.
77. Despotovic, M.; Nedic, V.; Despotovic, D.; Cvetanovic, S. Review and statistical analysis of different global solar radiation sunshine models. *Renew. Sustain. Energy Rev.* **2015**, *52*, 1869–1880. [CrossRef]
78. Gu, L.X.; Ding, F.X.; Fu, L.; Li, G. Mechanical behavior of concrete filled round ended steel tubular stub columns under axial load. *Chin. J. Highw. Transp.* **2014**, *27*, 57–63. (In Chinese)
79. Ren, Z.G.; Liu, C.; Wang, D.D.; Wei, W. Study on calculating method of ultimate bearing capacity of round-ended concrete filled steel tube short columns. *Build. Struct.* **2021**, *51*, 37–45. (In Chinese)
80. Ren, Z.G.; Zhang, L.; Li, Q. Research on axial compressive performance of ribbed round-ended rectangular concrete filled steel tubular short columns. *J. Wuhan Univ. Technol.* **2022**, *44*, 45–52. (In Chinese)
81. Xu, S.H. Research on Sectional Optimization of Round-Ended Rectangular Concrete-Filled Steel Tubular Stub Columns. Master's Thesis, Wuhan University of Technology, Wuhan, China, 2023. (In Chinese)
82. Ren, Z.G.; Wang, G.Y.; Li, P.P. Study on Bearing Capacity of Concrete-Filled Round Ended Steel Tubular Stub with Variable Center Angle Under Axial Compression. *J. Wuhan Univ. Technol.* **2020**, *42*, 29–36. (In Chinese)
83. Wang, D.D. Behavior Study on Compressive Behavior of Concrete-Filled Round-Ended Steel Tubular Stub Columns. Master's Thesis, Wuhan University of Technology, Wuhan, China, 2020. (In Chinese)